Sci. Technol. Arts Res. J., Oct. –Dec, 2025, 14(4), 142-152
DOI: https://doi.org/10.20372/star.V14.i4.10
ISSN: 2226-7522 (Print) and 2305-3372 (Online)
Science, Technology, and Arts Research Journal
Sci. Technol. Arts Res. J., Oct–Dec. 2025, 14(4), 142-152
Journal Homepage: https://journals.wgu.edu.et
Original Research

Effect of Holmium (III) Ion-Doped Nickel-Copper Ferrite Nanoparticle on Structural, Optical, and Dielectric Properties

Senbeto Kena Etana*
Department of Physics, College of Natural and Computational Sciences, Wollega University, Ethiopia

Abstract

This article examined the effect of Ho^{3+}-doped Nickel-Copper (Ni-Cu) ferrite nanoparticles on structural, optical, and dielectric parameters. XRD analysis revealed the structural retention in a single-phase cubic spinel structure. It demonstrated increasing Ho^{3+} ion concentration, with a decreased crystallite size ranging from 37.05 nm to 27.36 nm, mostly ascribed to ionic radii mismatch between the dopant and the pristine. Elemental composition of the sample was analyzed via Energy Dispersive X-ray spectroscopy, which confirms the sample's stoichiometric composition and good chemical purity. UV-Vis spectroscopy measurement revealed that the incorporation of Ho3+significantly reduced the band gap (Eg) from 2.486 electron volts to 2.128 electron volts. This decrease is ascribed to the development of Ho^{3+}-induced defect or impurity energy levels within the Ni-Cu ferrite's forbidden band gap, which enhances visible light absorption. Finally, impedance analysis confirmed the material's characteristic electrical response, revealing a sharp decrease in the real dielectric constant in the lower-frequency regions with applied field frequency, a relaxation phenomenon governed primarily by the Maxwell-Wagner interfacial polarization mechanism.

Article Information

Article History:
Received: 23-04-2024
Revised: 17-11-2025
Accepted: 31-12-2025

Keywords:
Nickel-Copper Ferrite, Dielectric Properties, Optical Properties, Sol-Gel Technique

*Corresponding Author:
Senbeto Kena Etana
E-mail:
senbkena@gmail.com

INTRODUCTION

Ferrite nanoparticles continue to draw global academic curiosity due to their versatile and useful applications in advanced fields such as energy storage, sophisticated drug delivery systems, electronic recording media, sensors, and actuators (Devsharma et al., 2024; Wasnik et al.,2023; Samani et al.,2023). Nickel-Copper (Ni-Cu) ferrite nanoparticles are considered cubic inverse spinel ferrites. The material's fundamental properties are dictated by its precise cation distribution, where Ni& Cu are preferentially occupied octahedral sites, while Fe exhibits a mixed distribution across both the tetrahedral and octahedral lattice positions (Mazurenko et al., 2024; Heni et al., 2025; Takallo et al., 2024; Sukumar et al., 2023; Taleb et al., 2024; Mulud et al., 2020). Sol-gel, co-precipitation, solid-state reaction, and microemulsion have been successfully applied to create Ni-Cu ferrites (Khoso et al., 2021; Ozçelik, 2023; Khasim et al., 2023). Whatever the preparation procedure, the resulting nanoparticle size can be accurately adjusted by modifying crucial process parameters such as concentration, temperature, and pH value. This nanoscale control is necessary because particle size has a direct impact on the material's stability, biocompatibility, and, most importantly, functional characteristics. Optimizing magnetic properties is crucial for applications such as Magnetic Resonance Imaging (MRI), which improves diagnostic accuracy, as well as tuning dielectric and

optical properties (Konnova & Rozhina, 2024; Umut et al., 2019; Eker et al., 2024; Mısırlıoğlu et al., 2024). The high dielectric constant and minimal energy loss of Ni-Cu ferrite nanoparticles make them excellent candidates for capacitors and filters (Priyadharsini et al., 2023; Khitouni & Sunol, 2024). Such characteristics are vital for improving device efficiency and reducing power waste.

Building on this known foundation, the current work proposes a novel approach: intentional inclusion of a trace amount of Holmium (Ho^{3+}) ions. The main goal is to optimize the material properties for Ni-Cu ferrite nanoparticles, resulting in improved performance potential for next-generation electrical and optoelectronic applications.

Statement of the Problem

Ferrite nanoparticles with nickel-copper (Ni-Cu) are well-known materials for high-frequency electronics due to their excellent magnetic and dielectric properties. However, achieving superior multifunctional performance, particularly the simultaneous optimization of structural stability, efficient optical absorption, and low-loss dielectric properties, remains a significant challenge for their use in next-generation optoelectronic devices and sensors. Specifically, while chemical substitution with rare-earth ions is widely accepted to modify ferrite properties through induced lattice strain and defect creation, there exists a critical gap regarding the comprehensive and quantitative effect of Holmium (Ho^{3+}) incorporation in the Ni-Cu spinel system. Without a thorough examination, the mechanisms by which Ho^{3+} affects the crystallite size, band gap energy (Eg) narrowing, and Maxwell-Wagner polarization behavior cannot be properly regulated. This study aims to address this problem by clarifying the precise structural and electronic relationship between Ho3+ doping concentration and the resulting modification of the structural integrity, optical response, and frequency-dependent dielectric of the host material.

Research Questions

1. How does the systematic incorporation of Holmium (Ho^{3+}) ions influence the host material properties? What specific structural mechanism, such as lattice strain, is responsible for the observed changes in morphology?
2. What effect does increasing Ho^{3+} doping concentration have on the energy band gap of Ni-Cu ferrite nanoparticles?
3. How do the Ho^{3+} insertions modify dielectric constants across the measured frequency range? Furthermore, how does the doping concentration influence the physical mechanism, specifically the Maxwell-Wagner interfacial polarization that governs the material's dielectric relaxation and loss behavior?

MATERIALS AND METHODS

The study utilized AR-grade precursors, all with a purity exceeding 99%. The metal nitrate sources included two moles of $Fe(NO_3)_3.9H_2O$, and one mole each of $Ni(NO_3)_2.6H_2$, $Cu(NO_3)_2.6H_2O$, and Holmium (III) nitrate penta hydrate ($Ho(NO_3)_3.5H_2O$). These were dissolved in doubly deionized water. Anhydrous citric acid ($C_6H_8O_7$) served as the chelating agent, while an ammonia solution (NH_3) was used for pH adjustment. Polyvinyl alcohol (PVA) was later employed as a binder during Pelletization.

The nitrate salt was first dissolved in doubly deionized water in a 150 ml beaker. An equal mole of anhydrous citric acid with the total mole of metal nitrates was then mixed and vigorously stirred via a magnetic stirrer. Subsequently, ammonia solution was added dropwise, adjusting the pH value to neutral. Heating the solution caused it to transform gradually into a clear, viscous sol, which eventually gelled into a structurally networked gel. This gel was dried on an evaporating plate in an oven set to 210^0C to remove moisture, yielding fluffy ash. To ensure the removal of remaining organic compounds and synthesis-related impurities, the

resultant ash was initially finely crushed with an agate mortar.

Finely ground calcined powder was divided for separate processing and characterization. A portion was mixed with a trace of PVA binder and compacted using a hydraulic press to form disk-shaped pellets. Samples were then placed in an alumina crucible and sintered for further densification in an electric furnace at a higher temperature of 700^0Cfor five hours. The fully sintered powder was then subjected to a thorough characterization process. The sample's crystal structure and phase purity were characterized via X-ray diffraction spectroscopy, while SEM characterizes surface morphology and particle aggregation. To achieve a reliable Ohmic contact, the sintered pellets were thoroughly polished and coated with silver paste before being dried for 30 minutes under a mercury arc and evaluated for dielectric qualities. Finally, UV-Vis spectroscopy was equipped to analyze the material's optical properties after the sintered powder was properly dissolved in an adequate organic solution.

Characterization Techniques

The finished sample underwent structural and phase investigation via X-ray Diffraction on an X'pert^3 PRO. This analysis used Cu Kα radiation (λ =1.542 Å) at room temperature. Using a 240 mm goniometric radius, the detector recorded X-ray reflections spanning the Bragg's angle range of $2\theta = 10^0$ to 70^0 (with the generator set to 40 kV and 30 mA) (Senbeto & Kebede, 2025; Kebede & Elangovan, 2024). The sample's surface morphology was studied via Scanning Electron Microscope (Model: JSM-7610F), creating signals from the sample through a focused stream of intense electrons. These signals offer topographical information by magnifying with high resolution. Elemental composition in the sample's compound was determined using EDX spectroscopy attached to SEM. This approach uses an electron beam to excite core electrons, resulting in the emission of characteristic X-ray peaks that correctly identify the elements in the sample (Guyett et al., 2024).

Optical properties of the synthesized sample were studied using a UV-Vis spectrometer (Shimadzu: UV-1800). Methanol has no absorbance in the wavelength range of 200 nm to 800 nm; thus, the sintered powder was first dissolved in this solvent. The solution was then placed in a cuvette holder, and the absorbance was measured over the necessary wavelength range, which is directly proportional to the transmitted light intensity. In parallel, the prepared sample's dielectric characteristics were examined using a Wayne Kerr Impedance Analyzer (Model 6500B) (Taleb et al., 2023). This was accomplished by placing the prepared pellet between the instrument's electrodes and measuring the complex impedance, which provided the essential information for determining the material's electrical properties.

RESULTS AND DISCUSSION

Results

XRD Analysis

Figure 1 (a-c) shows XRD patterns of confirmed synthesized samples of Ni-Cu ferrite doped with $Ho^{3+,}$ which possess a single-phase cubic structure, matching reference pattern CIF No. 5910028. Analysis utilizing the enhanced Rietveld Full Profile software (Wyckoff, 1964) confirmed this phase purity and high crystallinity. The XRD spectra exhibit sharp, well-defined peaks indexed to the characteristic Bragg angles for the spinel structure, specifically including reflections from the (111) ($\approx 18.2^0$), (220) ($\approx 30.2^0$), (311) ($\approx 35.5^0$), (400) ($\approx 43.1^0$), (422) ($\approx 53.5^0$), (511) ($\approx 57.1^0$), and (440) ($\approx 62.6^0$) planes.

Slight shifted XRD intense peaks to higher Bragg's angles (2θ), suggesting crystal distortion arose with the insertion of Ho^{3+} ions into the Fe^{3+} sites, giving rise to a detectable change in the unit cell's lattice parameters and crystallite size (D). This shift occurs without disrupting the fundamental cubic spinel phase, indicating successful substitution. To quantify these structural changes, the most intense peak (311) is used as the reference point for calculations. Table 1 contains the essential equations (1-5) necessary to precisely

determine the resulting crystallite size, the lattice constants, and X-ray density (ρ_x) of the Ho^{3+}-doped Ni-Cu ferrite nanoparticles.

The sample's crystallite size was calculated via the Scherrer formula as

$$D = \frac{k\lambda}{\beta Cos\theta} \quad (1)$$

The equation's variable λ defines X-ray wavelength, k refers to the Scherrer constant, $\beta$for Full width at Half Maximum (FWHM) of diffraction peak broadening, and θ is the glancing angle).

By Bragg's law, the glancing angle θ, the wavelength of the X-ray, and the crystal spacing corresponding to the (311) plane can be related:

$$2d_{hkl}Sin\theta = \lambda \quad (2)$$

The crystal d-spacing in a cubic crystal is mathematically linked to the lattice constant, a, and the volume of the unit cell through the following relationship:

$$a = d_{hkl}\sqrt{h^2 + k^2 + l^2} \quad (3)$$

$$V = a^3 \quad (4)$$

Sample'stheoretical density, which is often referred to as the X-ray density, is determined as follows:

$$\rho_{x-ray} = \frac{8M}{N_A V} \quad (5)$$

The variables are M, in this calculation referred to as the molecular weight of the compound, N_A as Avogadro's number, and V, as the volume of the unit cell.

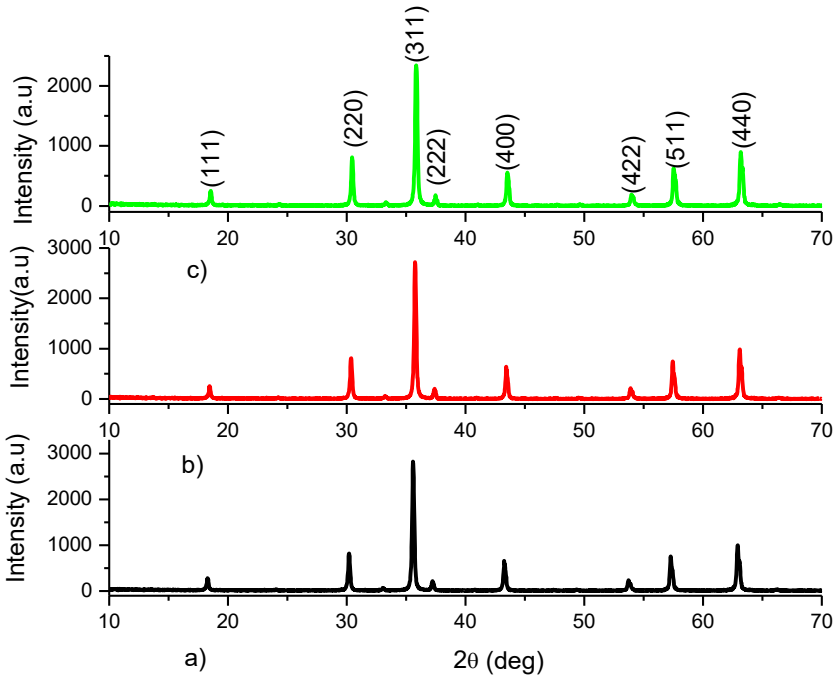

Figure 1 (a-c). *XRD pattern of* $Ni_{0.5}Cu_{0.5}Fe_{2-x}Ho_xO_4(x = 0, 0.03, 0.06)$

Discussions

Table 1 shows a decrease in crystallite size, D, and lattice constant a, with increasing Ho^{3+} dopant concentration. Conversely, the X-ray density (ρ_x) increases with rising Ho^{3+} content. Since the substituting ion, Holmium (III), has a larger ionic radius (1.041$\dot{A}$) than the ion it replaces, Iron (III) (0.645$\dot{A}$) at the octahedral (B-site), its incorporation introduces significant lattice strain into the crystal structure (Routray et al., 2025). This strain acts as a barrier to crystallite formation, preventing the aggregation of smaller particles into bigger crystallites, resulting in the observed reduction in crystallite size (D). The decrease in the overall lattice constant (a) despite the bigger Ho3+ ion shows that the substitution may potentially result in the creation of structural flaws or a subtle

rearrangement of cations, resulting in a net contraction of the unit cell edges.

Furthermore, the increase in X-ray density (ρ_x) is a direct consequence of the substitution of the lighter Fe^{3+}ion (Atomic Weight ≈55.85 g/mol) with the much heavier Ho^{3+} ion (Atomic Weight≈ 164.93 g/mol).

Morphology Studies

The SEM micrograph presented in Figure 2 for the Ho^{3+}doped Ni-Cu ferrite sample reveals that the synthesized nanoparticles exhibit significant agglomeration. The observed grouping of individual particles is fundamentally related to the structural alterations caused by the dopant. Holmium (III) ions with a higher ionic radius replace smaller Iron (III) ions, causing lattice deformation and strain in the crystal structure. The internal stress and lattice imperfections raise the nanoparticles' overall surface energy. The system seeks to achieve a lower, more stable energy state by decreasing its overall surface area, which is physically manifested as the spontaneous aggregation (agglomeration) of nearby nanoparticles. This agglomerated morphology, where numerous particles are physically clustered together, is a typical consequence of high surface activity and crystal lattice stress in doped ferrite systems, consistent with findings reported by other researchers (Sharma et al., 2021).

Table 1

Values of crystallite size (D), lattice constant (a), the volume of the unit cell (V), and X-ray density (ρ_{x-ray})

Sample	D(nm)	d-spacing (nm)	a(nm)	V(nm^3)	ρ_{x-ray} (g/cm^3)
$Ni_{0.5}Cu_{0.5}Fe_2O_4$	37.05	0.2522	0.8366	0.5854	5.3731
$Ni_{0.5}Cu_{0.5}Fe_{1.97}Ho_{0.03}O_4$	34.24	0.2521	0.8362	0.5847	5.4549
$Ni_{0.5}Cu_{0.5}Fe_{1.94}Ho_{0.06}O_4$	27.36	0.2515	0.8341	0.5804	5.5700

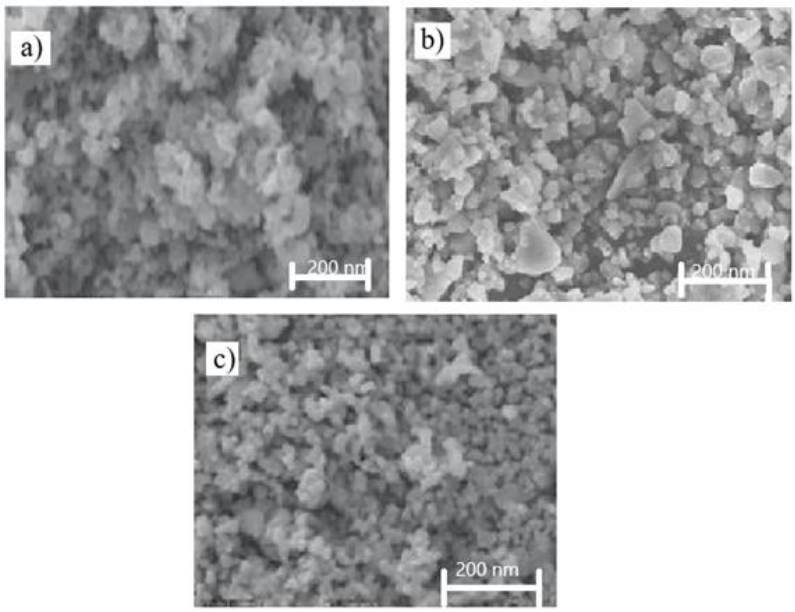

Figure 2. *SEM Micrograph of* $Ni_{0.5}Cu_{0.5}Fe_{2-x}Ho_xO_4(x = 0, 0.03, 0.06)$

The EDX spectrum displayed in Figure 3 confirmed the elemental composition of the Ho^{3+}-doped Ni-Cu ferrite sample. The analysis successfully identified all the expected constituent elements: Nickel (Ni), Copper (Cu), Holmium (Ho), Iron (Fe), and Oxygen (O). Crucially, the spectra reveal that the sample is free of any detectable impurities, supporting the high purity achieved during the synthesis process. Furthermore, as summarized in Table 2, the measured elemental ratios closely match the intended stoichiometry. ($(Ni_{0.5}\,Cu_{0.5}Fe_{2-x}Ho_xO_4)$, verifying that the desired composition was successfully realized.

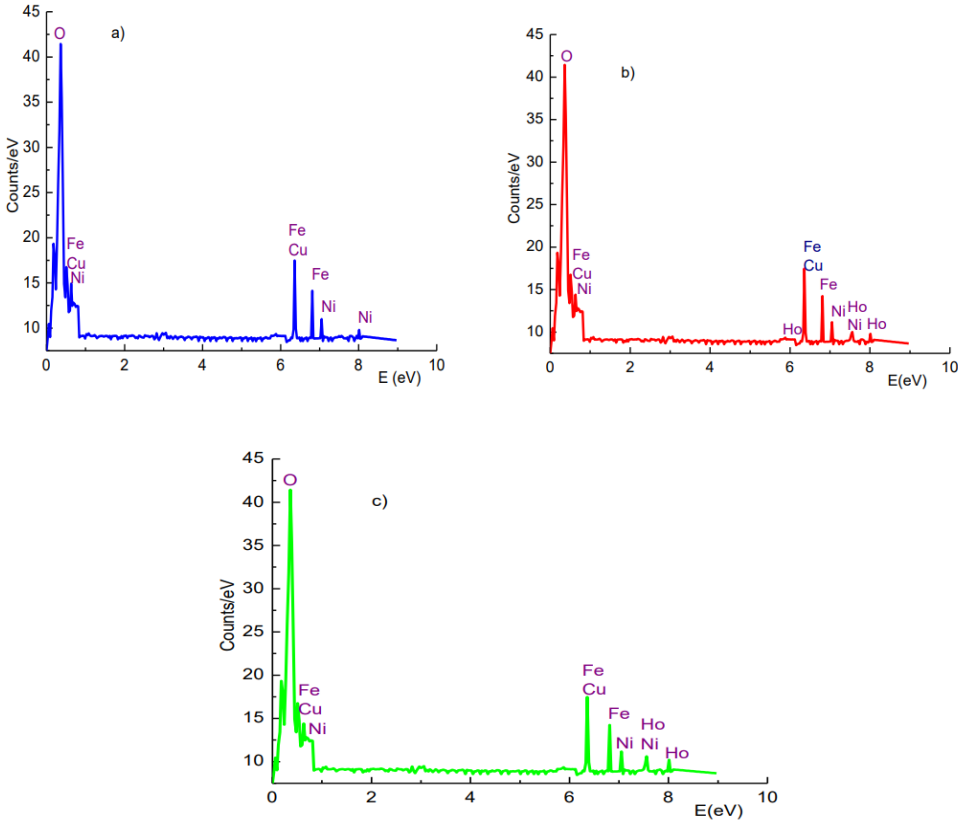

Figure 3 (a-c). *$Ni_{0.5}Cu_{0.5}Fe_{2-x}Ho_xO_4$,for a) x=0.0 , b) x=0.03 and c) x=0.06*

Table 2

Elemental composition sample for$Ni_{0.5}Cu_{0.5}Fe_{2-x}Ho_xO_4$ based on EDX Spectroscopy data

Element	x=0.00		x=0.03		x=0.06	
	At%	Wt%	At%	Wt%	At%	Wt%
O k	57.195	28.437	56.653	27.453	56.153	26.499
F L	28.537	46.195	28.325	44.608	28.077	43.062
Ni L	7.134	12.437	7.081	12.010	7.019	11.593
Cu L	7.134	12.880	7.081	12.439	7.019	12.007
Ho M	0.000	0.000	0.860	3.490	1.732	6.839
Total;	100	100	100	100	100	100

Optical Studies

The UV-Vis spectrum shown in Figure 4(a) presents the measured absorbance (A) as a function of wavelength (λ) for the series of Ho^{3+}-doped Ni-Cu ferrite nanoparticles at room temperature. This spectrum is the fundamental data used to understand the material's optical behavior, particularly its interaction with incident electromagnetic radiation.

To move from the raw absorbance data to a key optical parameter like the absorption coefficient (α), which is essential for determining the material's electronic band gap, the following relationship (often based on the Beer-Lambert law) is applied:

$$A = Log_{10}\left(\frac{I_o}{I}\right) \quad (7)$$

$$\alpha = 2.302\left(\frac{A}{L}\right) \quad (8)$$

Where I_o and I are the incident intensity of the photon on the sample and the transmitted intensity of the photon, respectively, and L represents the thickness of the sample holder (Cuvette in cm).

Direct band gap energy can be estimated from the Tauc plot, which is obtained from absorbance spectra data.

$$(\alpha h\nu)^2 = C(h\nu - E_g) \quad (9)$$

In this equation, α stands for absorption coefficient,

Figure 4 (b) illustrates the estimated band gap energy for $Ni_{0.5}Cu_{0.5}Fe_{2-x}Ho_xO_4$ sample from $(\alpha h\nu)^2$ versus hν plot by extrapolating a straight line where $(\alpha h\nu)^2=0$.

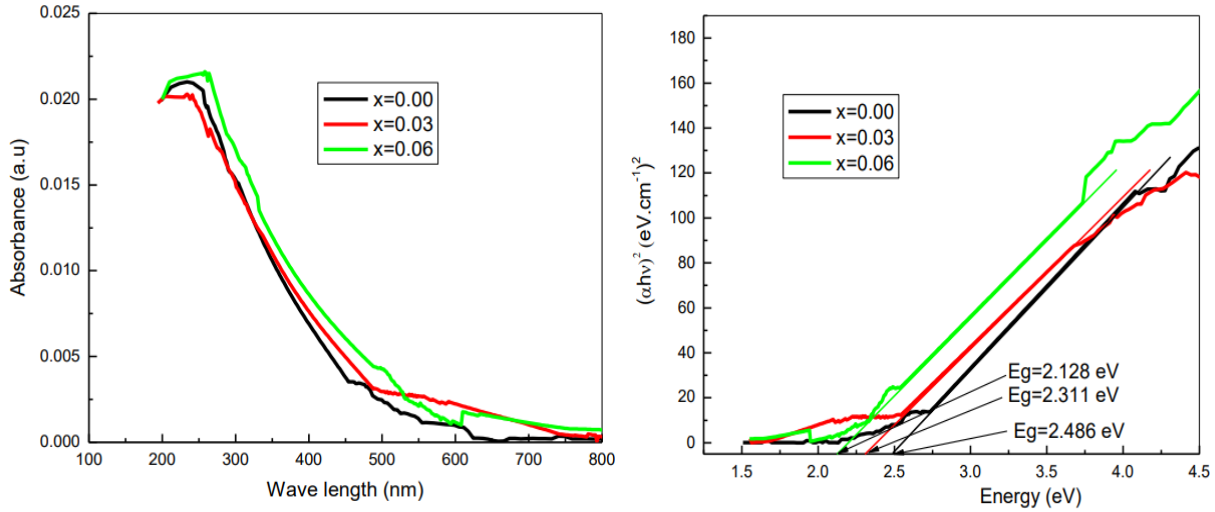

(a) (b)

Figure 4. *(a).Absorbance versus wavelength for* $Ni_{0.5}Cu_{0.5}Fe_{2-x}Ho_xO_4$
(b) The Tauc plot of $(\alpha h\nu)^2$ *versus* $h\nu$ *for* $Ni_{0.5}Cu_{0.5}Fe_{2-x}Ho_xO_4$

The Tauc plot presented in Figure 4(b) indicates a clear and significant decrease in band gap energy (Eg), ranging from 2.486 eV to 2.128 eV, with the Ho^{3+} concentration increases. Observed narrowing band gap energy (Eg) is fundamentally linked to the incorporation of Fe^{3+} ions with Ho^{3+} ions. This replacement perturbs ferrite's electronic structure, resulting in the development of new impurity energy states—or localized levels—within the material's forbidden gap. These newly formed levels effectively reduce the overall energy an electron requires to transition, resulting in the diminished Eg (Sinha & Dutta, 2020). An alternative influence is that the Ho^{3+} substitution may affect the oxidation state of $Fe^{3+}$and alter the density of states in the valence and conduction bands, which is consistent with the material exhibiting desirable properties like moderate

resistivity and minimal dielectric loss (Attia et al.,2022; Slimani et al., 2024).

Dielectric Studies

The analysis of the dielectric properties, as illustrated in Figure 5(a), shows that the real dielectric constant (ε') exhibits a characteristic frequency dispersion across the 1000 Hz to 1 MHz range. ε'decreases significantly in lower frequencies before stabilizing at a constant in the higher frequencies. This behavior is primarily governed by the Maxwell-Wagner interfacial polarization model. In low frequencies, charge carriers (such as those involved in Fe^{2+}/Fe3+ hopping) have sufficient time to accumulate at these resistive grain boundaries, creating a large space-charge polarization that results in the initial high value of ε'. In higher frequencies, the charge carriers lag behind the rapidly oscillating field, failing to accumulate at the interfaces, causing the contribution of interfacial polarization to drop sharply, thereby reducing the dielectric constant.

A similar relationship is observed in Figure 5(b), which plots the dielectric loss tangent (tanδ) against the logarithm of frequency (logf). The value of tan loss is high in lower frequencies and decreases with frequency. This correlation confirms that the same mechanism responsible for polarization, the movement and lagging of charge carriers, is also responsible for the energy losses. At low frequencies, the hopping mechanism contributes significantly to both polarization and conductivity loss. As the frequency increases and the charge carriers' movement becomes restricted, both the ability to polarize and the energy dissipated are reduced, validating the interdependent nature of the two dielectric parameters as they respond to frequency changes, which agrees with other work (Mubasher et al.,2024; Hegde et al., 2024).

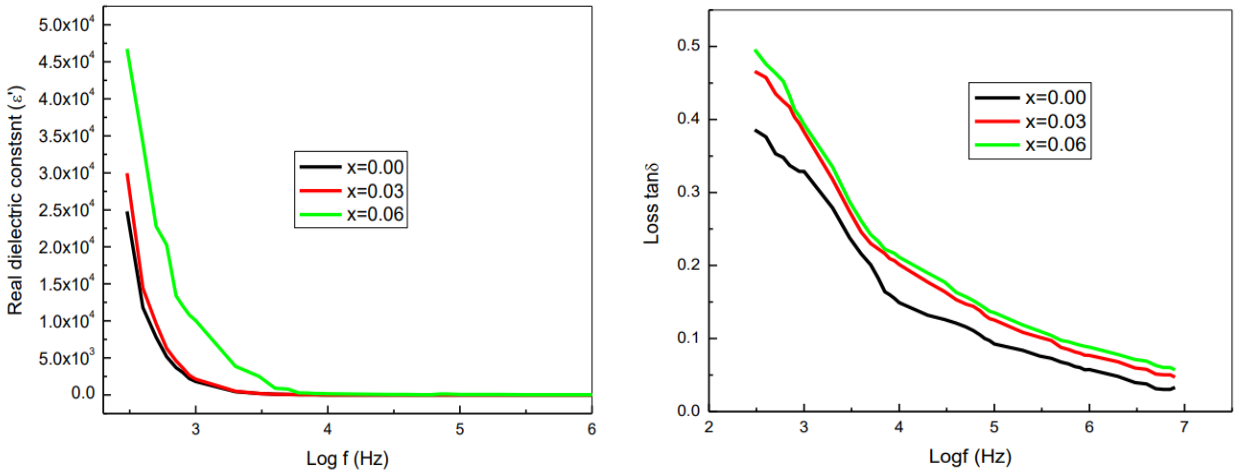

(a) (b)

Figure 5. *(a). Real dielectric constant versus Log f for* $Ni_{0.5}Cu_{0.5}Fe_{2-x}Ho_xO_4$
(b) Loss tangent versus Logf for $Ni_{0.5}Cu_{0.5}Fe_{2-x}Ho_xO_4$

CONCLUSIONS

This study successfully utilized the sol-gel method to synthesize Ho^{3+} doped Ni-Cu ferrite nanoparticles. XRD analysis confirmed a single-phase cubic spinel structure Fd3m across all samples. The increasing Ho^{3+} content caused the crystallite size, lattice constant, and unit cell volume to decrease, primarily due to the lattice strain from the Ho^{3+} ion, while the X-ray density increased. SEM confirmed particle agglomeration, and EDXverified high purity, matching the

intended stoichiometry (Fe, Ni, Cu, O, Ho). Optically, UV-Vis spectrometry showed the band gap energy (Eg) narrowed from 2.486 eV to 2.128 eV because of dopant-induced energy states within the band gap. Electrically, the dielectric constant decreased sharply with increasing frequency (Maxwell-Wagner mechanism), but doping increased the overall dielectric constant. These enhanced dielectric properties highlight the material's potential for applications in sensors, energy storage, and communication technology.

Recommendation

Future work should prioritize exploring alternative synthesis methods, such as hydrothermal or co-precipitation, to reduce the observed particle agglomeration and achieve a more uniform particle size distribution. A critical next step is to conduct a detailed study of the magnetic properties, like saturation magnetization and coercivity, which were not covered here, to assess the material's potential for data storage and sensing applications. Additionally, advanced complex impedance spectroscopy is recommended to precisely model the Maxwell-Wagner relaxation and decouple the contributions of grains and grain boundaries, thus providing the robust understanding necessary for optimizing the dielectric performance for technological applications.

CRediT Authorship Contribution Statement

The author confirms they are the sole creator and are responsible for all aspects of this work, including conception, data analysis, and manuscript preparation.

Declaration of competing interest

The author declares no conflict of interest.

Ethical approval

Not applicable

Data availability

The scientific data used for this research are available upon request from the corresponding author.

Acknowledgement

The author is grateful to the Department of Physics at Wollega University for its support in completing this study.

REFERENCES

Attia, S., Helaili, N., Rekhila, G., Bessekhouad, Y., & Trari, M. (2022). Physical and photo-electrochemical properties of the spinel SrFe2O4: application to hydrogen production under visible light. *Journal of Materials Science Materials in Electronics*, *33*(13), 9976–9987. https://doi.org/10.1007/s10854-022-07989-1

Devsharma, S. C., Rahman, M. L., Hossain, M. J., Biswas, B., Ahmed, M. F., & Sharmin, N. (2024). Elucidation of structural, electromagnetic, and optical properties of Cu–Mg ferrite nanoparticles. *Heliyon*, *10* (13), e33 578. https://doi.org/10.1016/j.heliyon.2024.e33578

Eker, F., Duman, H., Akdaşçi, E., Bolat, E., Sarıtaş, S., Karav, S., & Witkowska, A. M. (2024). A comprehensive review of nanoparticles: from classification to application and toxicity. *Molecules*, *29* (15), 3482. https://doi.org/10.3390/molecules29153482

Guyett, P. C., Chew, D., Azevedo, V., Blennerhassett, L. C., Rosca, C., & Tomlinson, E. (2024). Optimizing SEM-EDX for fast, high-quality, and non-destructive elemental analysis of glass. *Journal of Analytical Atomic Spectrometry*, *39* (10), 2565–2579. https://doi.org/10.1039/d4ja00212a

Hegde, V. N., Manju, V. V., & Hemaraju, B. C. (2024). Frequency and temperature-dependent dielectric properties of CuO nanoparticles. *Chemical Physics Impact*, *8*, 100474. https://doi.org/10.1016/j.chphi.2024.100474

Heni, S., Rhouma, F. I. H., Hcini, S., Knani, S., Dhahri, A., Hlil, E. K., Gassoumi, M., & Khirouni, K. (2025). Structural, cation distribution, optical, and magnetic properties of Sol-Gel synthesized NI0.5CU0.5FE2O4 ferrite nanoparticles for optoelectronic and

microwave devices. *Journal of Materials Engineering and Performance*. *34 (2),* 1-17. https://doi.org/10.1007/s11665-025-12896-7

Kebede, L., & Elangovan, S. (2024). Dielectric properties of (1 − x) PMN–(x) AB ceramic nano powder. *Advances in Applied Ceramics Structural Functional and Bioceramics*, *123* (4–6), 90–96. https://doi.org/10.1177/17436753241302223

Khasim, S., Ramakrishna, B. N., Pasha, A., & Manjunatha, S. O. (2023). Structural, optical, magnetic, and electrical properties of samarium (Sm3+)-doped copper–iron oxide ferrites for possible optoelectronic applications. *Journal of Electronic Materials*, *53*(2), 801–814. https://doi.org/10.1007/s11664-023-10797-w

Khitouni, M., & Suñol, J. (2024). Magnetic, dielectric, electrical, optical, and thermal properties of crystalline materials. *Crystals*, *14* (252), 1-4. https://doi.org/10.3390/cryst14030252

Khoso, W. A., Haleem, N., Baig, M. A., & Jamal, Y. (2021). Synthesis, characterization, and heavy metal removal efficiency of nickel ferrite nanoparticles (NFN's). *Scientific Reports*, *11*(1), 3790. https://doi.org/10.1038/s41598-021-83363-1

Konnova, S., & Rozhina, E. (2024). Magnetic Nanoparticles for Biomedical and Imaging Applications. *International Journal of Molecular Sciences*, 25(11), 5847. https://doi.org/10.3390/ijms25115847

Mazurenko, J., K, S. A., Kaykan, L., Michalik, J. M., Gondek, L., Szostak, E., & Antoni, Ż. (2025). Impact of cation distribution in shaping the structural and magnetic characteristics of Ni-Cu ferrite. *Physica Scripta*, *100*(3), 035940. https://doi.org/10.1088/1402-4896/adb2c3

Mısırlıoğlu, B. S., Kahya, N. D., &Öztürk, Z. (2024). Enhanced dielectric properties of coppersubstituted nickel ferrite nanoparticles for energy storage applications. *Journal of Physics and Chemistry of Solids*, *193*, 112195. https://doi.org/10.1016/j.jpcs.2024.112195

Mubasher, N., Mumtaz, M., Ali, H., Tariq, H. U., Ahmed, M., Ilyas, A., Inam-Ul-Haq, M., & Shahzad, M. F. (2024b). Effect of lithium doping on frequency-dependent dielectric properties of manganese ferrite nanoparticles. *Applied Physics A*, *130*(2), 1-10. https://doi.org/10.1007/s00339-023-07251-3

Mulud, F. H., Dahham, N. A., &Waheed, I. F. (2020). Synthesis and characterization of copper ferrite nanoparticles. *IOP Conference Series Materials Science and Engineering*, *928*(7), 072125. https://doi.org/10.1088/1757-899x/928/7/072125

Ozçelik, S. (2023). Copper ferrite nanoparticles: structural, magnetic, optical, photocatalytic activity and blood compatibility properties. *BioNanoScience*, *13*(3), 958–972. https://doi.org/10.1007/s12668-023-01130-0

Priyadharsini, R., Manoharan, C., Bououdina, M., Sagadevan, S., Venkateshwarlu, M., & Bahadur, S. A. (2023). Impact of nickel substitution on structural, dielectric, magnetic, and electrochemical properties of copper ferrite nanostructures for energy storage devices. *Journal of Colloid and Interface Science*, *653*, 917–929. https://doi.org/10.1016/j.jcis.2023.09.113

Routray, S., Pradhan, S. K., Parida, B. N., & Das, R. (2025). Effect of holmium doping on structural, optical, dielectric and magnetic properties of cobalt ferrite. *Bulletin of Materials Science*, 48(1), 12. https://doi.org/10.1007/s12034-024-03385-z

Samani, M. S., Sharifi, H., Sharifi, I., Mobarakeh, S. A. E., &Isfahani, T. (2023). Effect of Cu doping on the structural and magnetic properties of MnFe2O4 nanoparticles. *Applied Physics A*, *129*(5), 319. .https://doi.org/10.1007/s00339-023-06503-6

Senbeto, K. &. Kebede, L. (2025). Investigation of structural, optical, and magnetic properties of ytterbium-aluminum ions co-doped bismuth ferrite nano-ceramics. *Science, Technology and Arts Research Journal*, *14*(3), 134–143. https://doi.org/10.20372/star.v14.i3.11

Sharma, S., Verma, M. K., Sharma, N. D., Choudhary, N., Singh, S., & Singh, D. (2021).

Rare- earth doped Ni–Co ferrites synthesized by Pechini method: Cation distribution and high temperature magnetic studies. *Ceramics International*, *47*(12), 17510–17519. https://doi.org/10.1016/j.ceramint.2021.03.069

Sinha, A., & Dutta, A. (2020). Structural, optical, and electrical transport properties of some rare-earth-doped nickel ferrites: A study on effect of ionic radii of dopants. *Journal of Physics and Chemistry of Solids*, *145*, 109534. https://doi.org/10.1016/j.jpcs.2020.109534

Slimani, Y., Almessiere, M. A., Baykal, A., Klygach, D. S., Trukhanov, S. V., Trukhanov, A. V., and Ul-Hamid, A.(2024). Structural, magnetic, electromagnetic, and hyperfine interactions of rare earth Ho doped in mixed Co–Ni spinel ferrites. Journal of *Applied Physics A, 131 (6),* 1-17. https://doi.org/10.1007/s00339-025-08493-x

Sukumar, M., Rajabathar, J. R., Al-Lohedan, H., Suresh, S., Dash, C. S., Sundararajan, M., Subudhi, P. S., Arokiyaraj, S., Yanmaz, E., Yuvaraj, S., & Isaac, R. R. (2023). Synthesize and characterization of copper doped nickel ferrite nanoparticles effect on magnetic properties and visible light catalysis for rhodamine dye degradation mechanism. *Journal of Alloys and Compounds*, *953*, 169902. https://doi.org/10.1016/j.jallcom.2023.169902

Takalloo, F., Gholizadeh, A., & Ardyanian, M. (2024). Crystal structure-physical properties correlation in Ni–Cu–Zn spinel ferrite. *Journal of Materials Science Materials in Electronics*, *35* (27), 1792. https://doi.org/10.1007/s10854-024-13574-5

Taleb, M. F. A., Ibrahim, M. M., Rahman, A., & El-Bahy, Z. M. (2024). Magnetic response of Ho^{3+} doped $Ni_{0.4}Cu_{0.6}Ho_yFe_{2-y}O_4$ spinel ferrites and their correlation with crystallite size. *Ceramics International*, *50* (19), 37077--37084. https://doi.org/10.1016/j.ceramint.2024.07.096

Taleb, N. I., Saci, A., Chebout, M., & Bendouani, S. (2023). A complete review on UV-visible spectroscopic technique. *International Journal of Research and Development in Pharmacy and Life Sciences, 12* (4), 1–9. https://doi.org/10.35629/7781-070612881299

Umut, E., Coşkun, M., Pineider, F., Berti, D., & Güngüneş, H. (2019). Nickel ferrite nanoparticles for simultaneous use in magnetic resonance imaging and magnetic fluid hyperthermia. *Journal of Colloid and Interface Science*, *550*, 199–209. https://doi.org/10.1016/j.jcis.2019.04.092

Wasnik, P. B., Rokade, S. D., & Rewatkar, K. G. (2023). Review Paper on Ni-Cu ferrite. *Proceedings of the National Academy of Sciences India Section A: Physical Sciences*, *93* (3), 517–523. https://doi.org/10.1007/s40010-023-00844-w

Wyckoff. (1964). Crystallography Open Database: Information card for entry 5910028. (n.d.). https://www.crystallography.net/cod/5910028.html